Enhancing Photocatalytic CO_2 Reduction via a Single-Domain Ferroelectric Z-scheme Heterojunction of $BiFeO_3$/$CsPbBr_3$ Inducing Dual Built-in Electric Fields

Danrui Pan, [a] *Yi Lu,* [a] *Ahmed Mahmoud Idris,* [b]* *Zhihao Chen* [a], *Leyi Xu,* [a] *Jin Wang,* [a,c] *Guocan Jiang,* [a,b] *Zhaojiang Chen,* [b]* *Zhengquan Li* [a,c]*

[a] *Key Laboratory of the Ministry of Education for Advanced Catalysis Materials, Zhejiang Normal University, Jinhua, Zhejiang 321004, China*

[b] *Zhejiang Normal University School of Physics and Electronic Information Engineering, Jinhua, Zhejiang 321004, China*

[c] *Zhejiang Institute of Photoelectronic, Zhejiang Normal University, Jinhua, Zhejiang 321004, China*

* *Corresponding authors. E-mail addresses: ahmed503@zjnu.edu.cn (A. M. Idris), zjchen@zjnu.edu.cn (Z. Chen), zqli@zjnu.edu.cn (Z. Li).*

1. Chemical and reagent

All chemicals and reagents were of analytical grade and used as purchased without any further purification. $Bi(NO_3)_3 \cdot 5H_2O$ (99%, Aladdin); $FeCl_3 \cdot 6H_2O$ (99%, Aladdin); Cs_2CO_3 (99.99%, Aladdin); $PbBr_2$ (99.0%, Aladdin); $NH_3 \cdot H_2O$ (Sinopharm Chemical); NaOH (Sinopharm Chemical); 1-octadecene (>90.0%, Aladdin); oleic acid (90%, Aladdin); oleyl amine (90%, Aladdin); H_2PtCl_6 (99.995%, Aladdin); ethyl acetate (99.8%, Aladdin) The deionized water used for the experiments was purified by a Millipore Milli-Q system.

2. Samples Characterizations

Transmission electron microscopy (TEM) and high-resolution TEM (HRTEM) were performed on a JEOL 2010F transmission electron microscope operated at 200 kV.. scanning electron microscopy (SEM) and energy dispersive X-ray spectroscopy (EDX) were performed on a Hitachi S-4800 Scanning electron microscope. The atomic force microscopy (AFM) image was collected on an AFM (Bruker Multimode 8, USA) in scan analyst mode. X-ray diffraction measurements (XRD) were carried out at room temperature using a Philips X' Pert Pro X-ray diffractometer with Cu Kα radiation. UV-vis diffuse reflectance spectra (DRS) were recorded on an Agilent-Cary 5000 spectrometer equipped with an integrating sphere. Zeta potential was obtained using a Zeta sizer Nano-ZS (Malvern Instruments, U.K.). X-ray photoelectron spectroscopy (XPS) and valence band spectra were measured on an ESCA Lab MKII X-ray photoelectron spectrometer equipped with Al-Kα X-ray radiation. Ultraviolet photoelectron spectroscopy (UPS) was collected on Thermo Scientific ESCALab 250Xi with a photon energy of 21.2 eV as the excitation source. Steady-state photoluminescence (PL) spectra were recorded on a Hitachi H-4600 spectrometer equipped with an Xe lamp. Time-resolved PL (TRPL) decay spectra were recorded (FLS980, Edinburgh Instruments Ltd) with the time-correlated single-photon counting (TCSPC) mode. Electron paramagnetic resonance (EPR) was measured using the Bruker EPR EMXplus. 5,5-dimethyl-1-pyrroline N-oxide (DMPO) was employed as a radical trapping reagent to capture oxygen radicals under light illumination. The samples were operated in a glove box to maintain a vacuum. CO_2 adsorption isotherms were measured using the ASAP 2020 HD88 sorption analyzer at 25 ℃. *In-situ* infrared Fourier Transform spectra (FTIR) measurements were recorded using a Nicolet iS50 FTIR spectrometer (Thermo). The sample was placed in the center of the in-situ cell. Collect background information at room temperature. The in-situ reaction cell was purged with a CO_2 gas stream and H_2O, and the signal was collected at the same time interval after the adsorption equilibrium. Differential scanning calorimetry (DSC) was recorded (DSC STA449F5) to investigate the phase transition properties under a

nitrogen atmosphere with a flow rate of 60 mL min^{-1}. The measurement uncertainties are within ±0.1℃ (Standard metal) and ±1% for the temperature and enthalpy, respectively. The samples were heated from room temperature to 900 ℃ at the scanning rate of 10 ℃ min^{-1} to analyze the phase change properties.

The surface photovoltage spectra (SPV) were obtained on a surface photovoltage spectrometer (PLSPS/IPCE1000, Beijing Perfect Light Technology Co., Ltd.)., which is made of a monochromatic light source with a mechanical chopper (SR540, Stanford research, Inc.) and a lock-in amplifier (SR830-DSP). The intensity of the internal electric field values of the BFO NSs, CPB NCs, and BFO/CPB heterojunction were measured using the formula:[1]

$$F = (-2V\rho/\varepsilon\varepsilon_0)^{1/2}$$

where F is the internal electric field magnitude, V is the surface voltage, ρ is the surface charge density, ε is the low-frequency dielectric constant, and ε_0 is the permittivity of free space.

3. Photoelectrochemical measurements

Photocurrent responses and electrochemical impedance spectroscopy (EIS) measurements were performed on a three-electrode system CHI 660D electrochemistry workstation (Shanghai Chenhua, China) using a sample-coated FTO glass as photoelectrode, a Pt foil as counter electrode and an Ag/AgCl electrode as reference electrode, respectively. The working electrode was prepared by dipping method, where 2 mg of catalyst was ultrasonically dispersed in 50 μL of ethyl acetate and then deposited on FTO conductive glass with an exposed surface area of about 0.98 cm^{-2}. Then a mixture of acetonitrile and ethyl acetate (v: v, 1:15) containing 0.1 M of tetrabutylammonium hexafluorophosphate (TBAPF6) was used as the electrolyte. The variation of photoinduced current density versus time (I-t curve) was recorded at a 0 V bias potential under light switching on and off mode, λ > 400 nm, 300 W Xe lamp (Solaredge 700). The electrochemical impedance spectroscopy (EIS) results were obtained at the open circuit potential using a frequency ranged from 10^4 Hz to 10^{-1} Hz.

Polarization electric-field hysteresis loop and Leak current were obtained on a Radiant Precision Multiferroic Materials analyzer. The powder sample was pressed under pressure at 15 MPa to obtain a round sheet with a diameter of 1 cm and a thickness of 1 mm.[2] Then the as-prepared round sheet was plated with Ag as an electrode on the upper and lower surfaces to connecting wires at both ends.

4. DFT simulations

The DFT simulation was carried out by the Vienna Ab-initio Simulation Package (VASP).[3] The projector-augmented wave (PAW) pseudopotentials method was utilized to describe the electron-ion interactions.[4] The generalized gradient approximation (GGA) was used with Perdew–Burke–Ernzerhof (PBE) to perform the exchange and to correlate the functional. Since CPB has Br defects, the effects of Br defects are considered in the Gibbs free energy (ΔG) calculation. A supercell CPB (200) surface and a supercell BFO (110) surface were used for calculations, respectively. The Monkhorst-Pack grid mesh-based Brillouin zone k-points are set as 2×2×1 for all surface structures with the cutoff energy of 450 eV and the equilibrium was reached when the forces on the relaxed atoms became less than 0.05 eV/Å. A 20 Å vacuum layer along the Z direction is employed.

5. Photocatalytic CO_2 reduction

The photocatalytic CO_2 reduction experiments were performed in the solid-vapor reaction system using a Pyrex photoreactor containing saturated CO_2 and photocatalyst. A 300 W Xe lamp (PLS-SXE300, Beijing Perfect-light) with a power density of 150 mW cm^{-2} covered with a 420 nm cut-off filter was used as a light source. Typicaly, 5 mg of the prepared photocatalyst was evenly coated on glass and put into a 20 mL of Pyrex photoreactor with 50 μL DI water. The photoreactor was sealed with a rubber septum and purged with high purity CO_2 for 10 min in the dark. Subsequent, the photoreactor was irradiated with light. The gas products were qualitatively analyzed by an Agilent GC-7820A gas chromatograph equipped with flame ionization detector

(FID), thermal conductivity detector (TCD) and nickel reformer furnace.

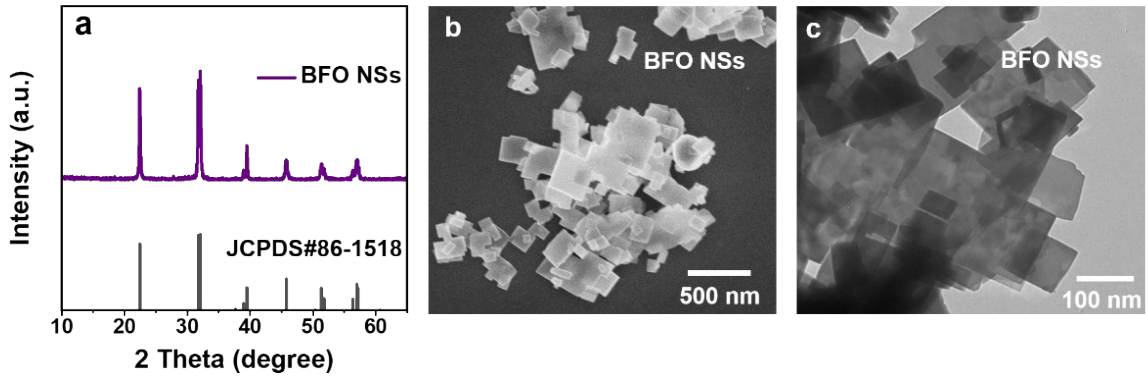

Fig. S1 (a) XRD pattern, (b) SEM image, and (c) TEM image of as-prepared pristine BFO NSs.

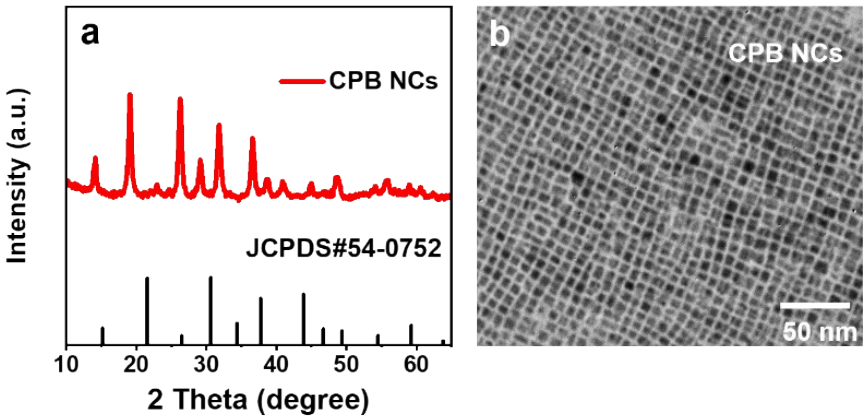

Fig. S2 (a) XRD pattern and (b)TEM image of as-prepared CPB NCs.

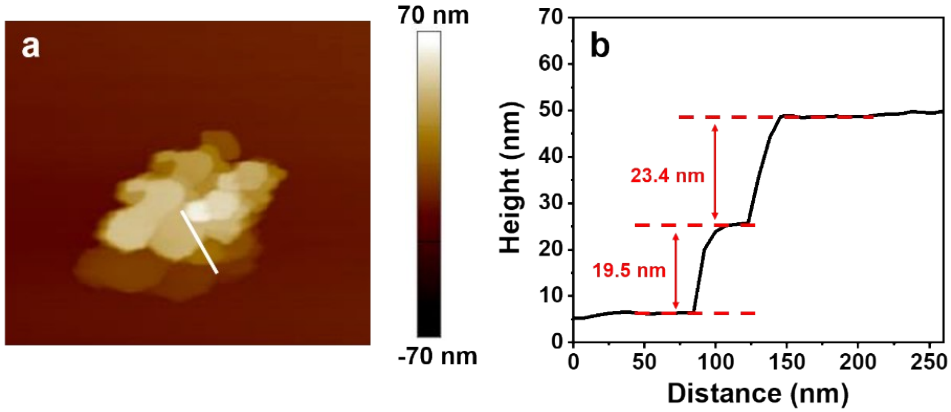

Fig. S3 (a and b) AFM image and corresponding height profiles of as-prepared BFO NSs, receptively.

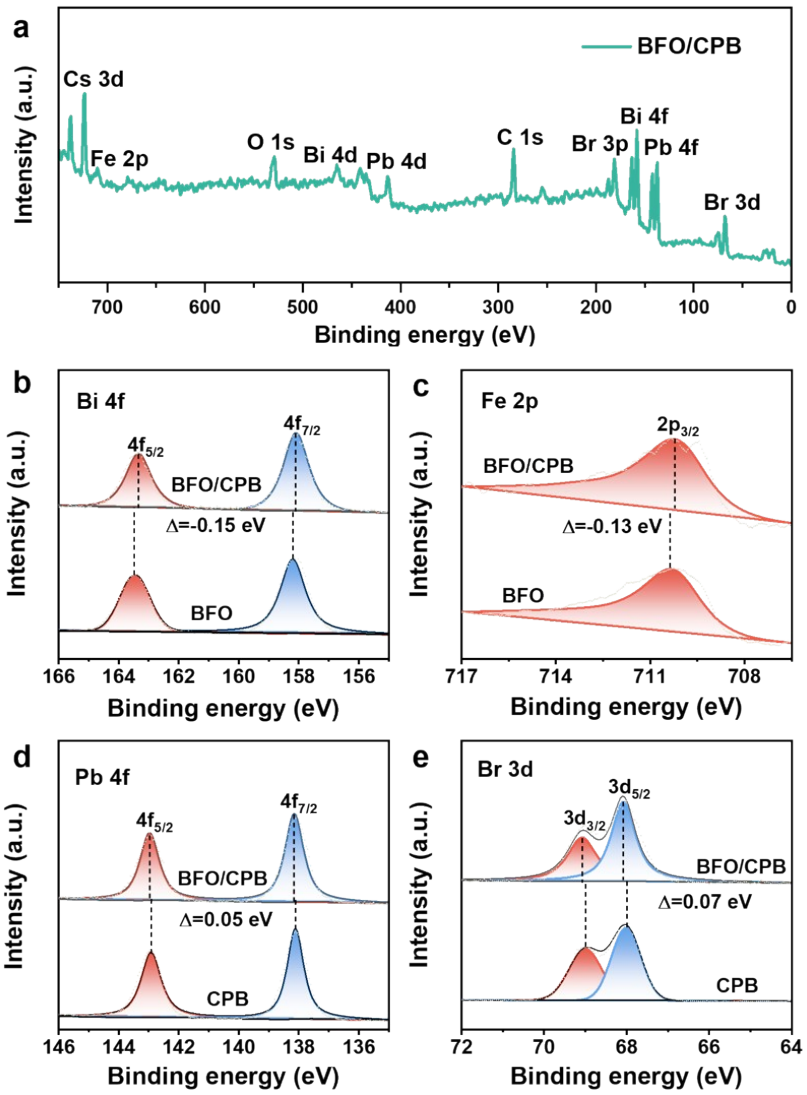

Fig. S4 (a) XPS survey spectra of BFO/CPB heterojunction. High-resolution XPS spectra of Bi 4f (b), Fe 2p (c), Pb 4f (d), and Br 3d (e).

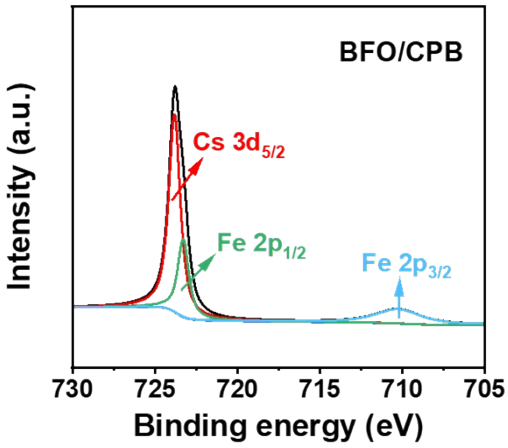

Fig. S5 High-resolution XPS spectra of Cs 3d and Fe 2p.

The Fe 2p spectrum from BFO can be divided into two typical splitting peaks at 710.2 eV and 723.3 eV, where are ascribed to Fe $2p_{3/2}$ and Fe $2p_{1/2}$[3]. Since the positions of Cs $3d_{5/2}$ and Fe $2p_{1/2}$ almost coincide, we use Fe $2p_{3/2}$ to represent Fe 2p.

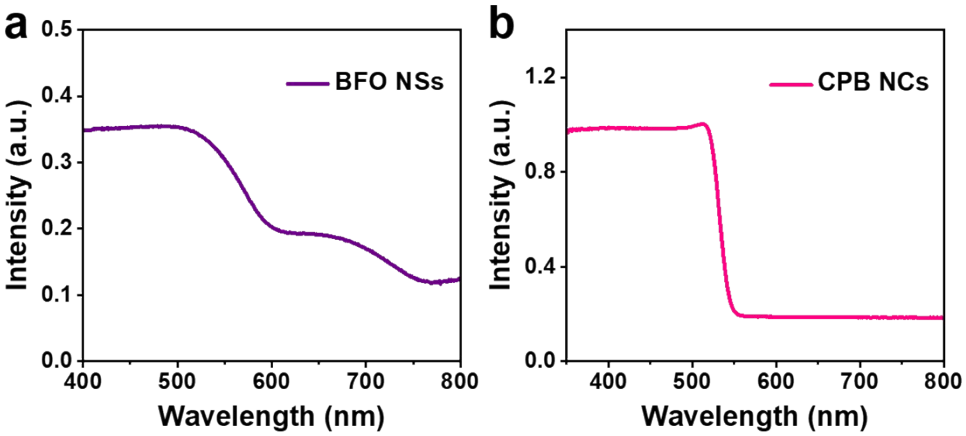

Fig. S6 (a and b) UV−vis diffuse reflectance spectroscopy (DRS) of the pristine BFO NSs and CPB NCs.

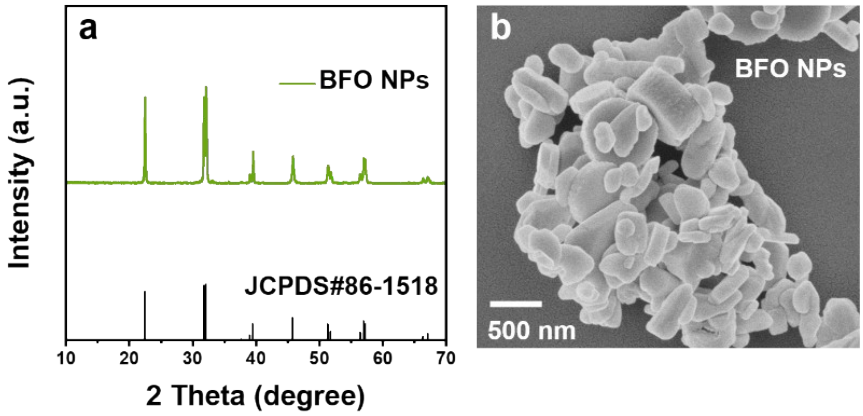

Fig. S7 (a) XRD pattern and (b) SEM image of the BFO NPs.

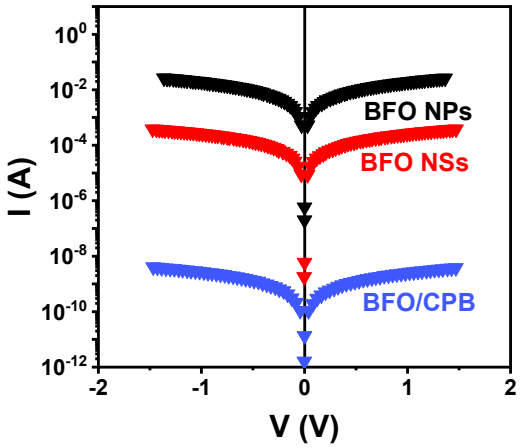

Fig. S8 Leakage current behavior of BFO NSs, BFO NPs and BFO/CPB heterojunction.

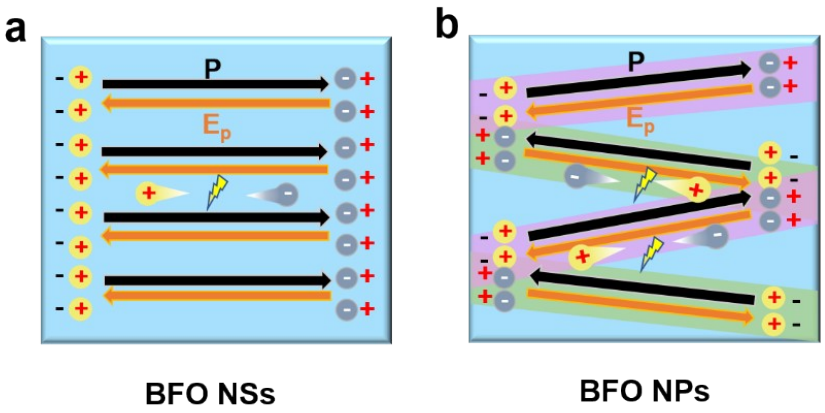

Fig. S9 (a and b) Single-domain and polydomain structure of BFO, respectively.

The polarized electric fields inside single-domain BFO NSs are in the same directions, forming positive and negative polar surfaces inside the material. When illuminated, photogenerated electrons and holes migrate to positive and negative polarity surfaces, respectively. In contrast, the polarized electric fields direction inside polydomain structure of BFO NPs are disorderly, and the recombination of electrons and holes will inevitably occur during the migration to the polar surface under illumination, so the carrier separation effect is not ideal.

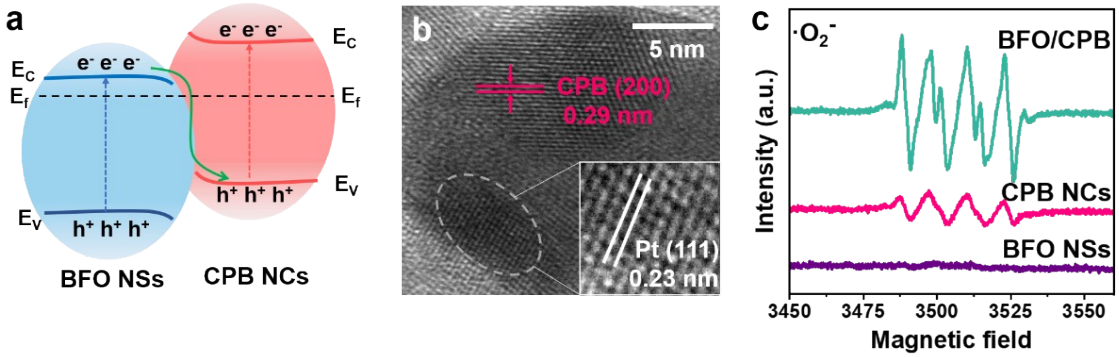

Fig. S10 (a) Schematic illustration of the Z-scheme charges transfer mode within the BFO/CPB heterojunction. (b) HRTEM of photodeposited Pt nanoparticles on the surface of BFO/CPB heterojunction. (c) ESR spectra of BFO NSs, CPB NCs and BFO/CPB heterojunction.

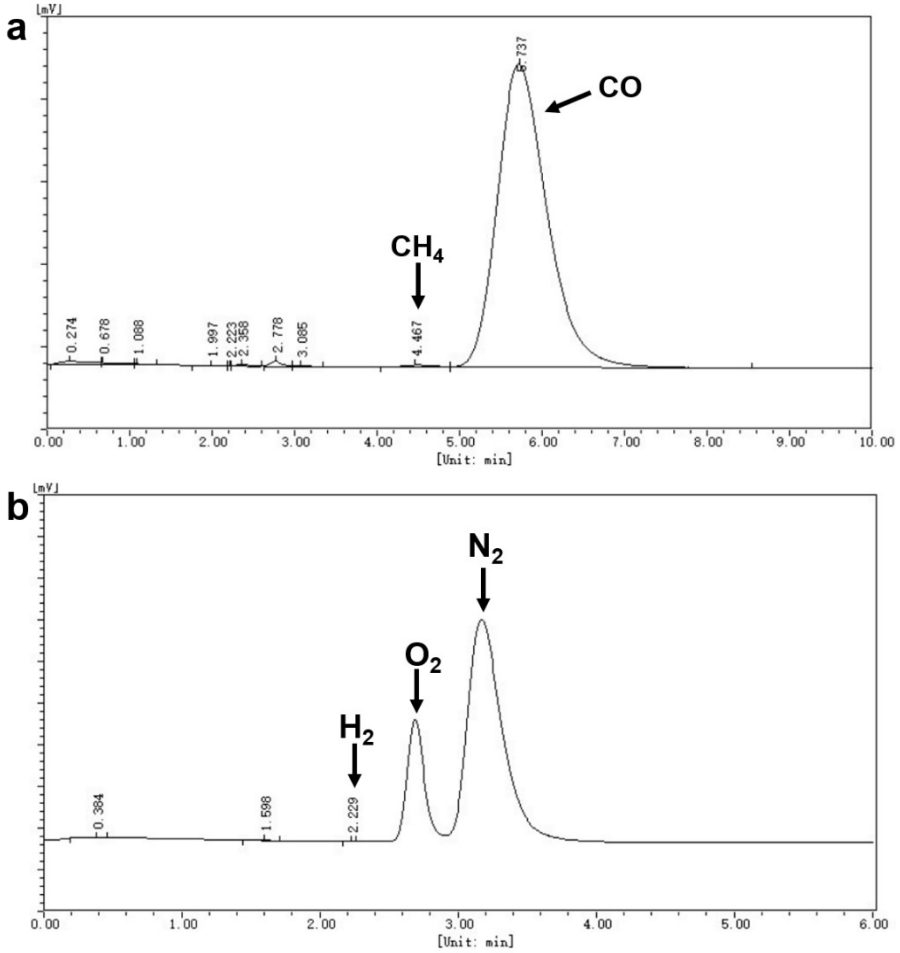

Fig. S11 The original GC graph from (a) FID detector and (b) TCD detector.

The GC results in Figure S11 (a and b) showed that in our solid-vapor reaction system, the main product of photocatalytic CO_2 reduction was CO, with only very small amounts of CH_4 was detected, and no H_2 was detected.

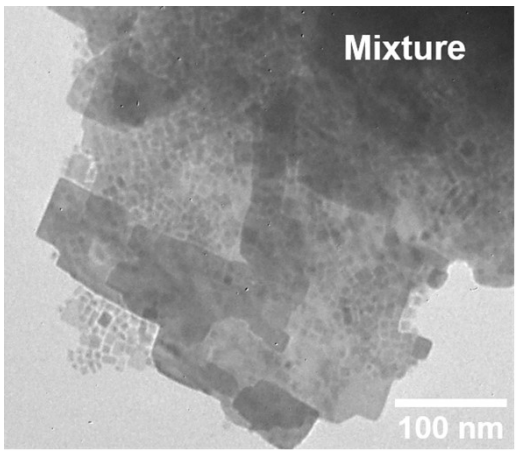

Fig. S12 TEM image of the Mixture of BFO NSs and CPB NCs.

It can be seen from the Fig. S11 that the boundary between BFO NSs and CPB NCs is not clear and the contact is not ideal, indicating that the interfacial charge transport efficiency of the mixture is low.

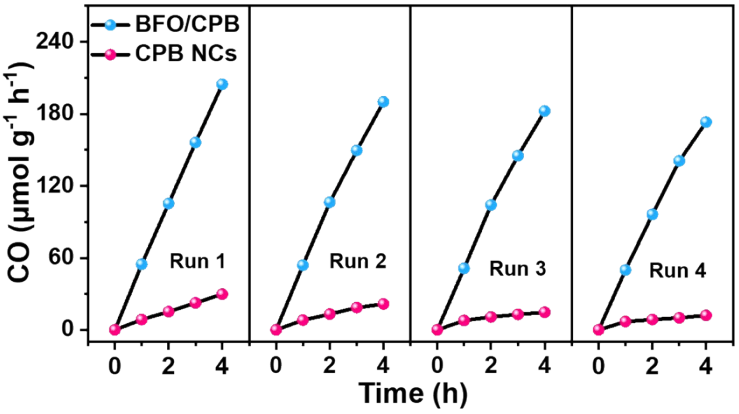

Fig. S13 Photocatalytic durability test over BFO/CPB and CPB NCs with four 4-h cycles.

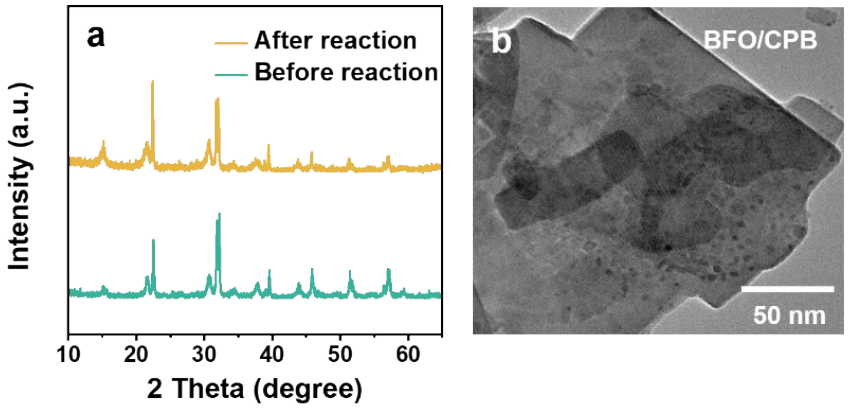

Fig. S14 (a) XRD pattern and (b)TEM image of BFO/CPB heterojunction after photocatalytic reactions.

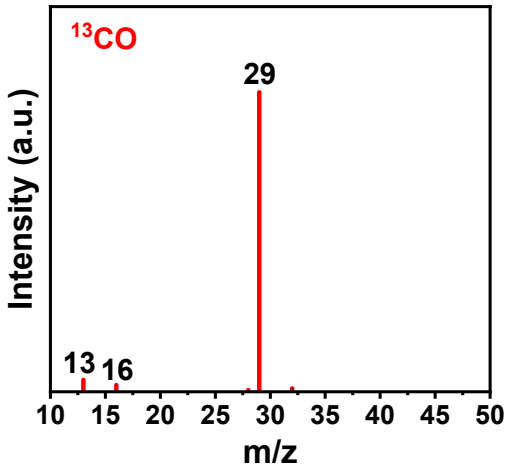

Fig. S15 Mass spectra showing ^{13}CO (m/z = 29) produced over BFO/CPB heterojunction in the photocatalytic reduction of $^{13}CO_2$.

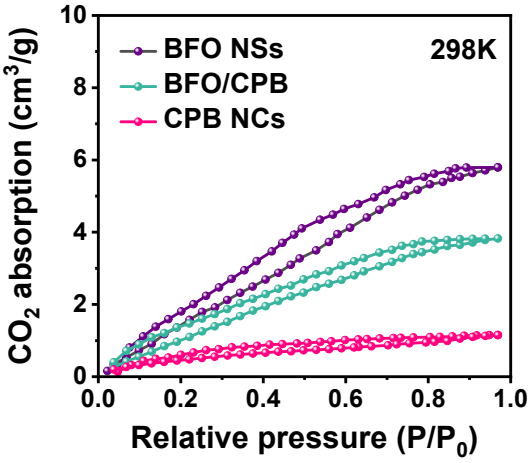

Fig. S16 CO_2 adsorption isotherms of BFO NSs, CPB NCs and BFO/CPB heterojunction at 298 K.

The results in Fig. S16 reveal that BFO NSs exhibit a higher CO_2 adsorption capacity compared to pristine CPB NCs. In contrast, the BFO/CPB heterojunction showed an improved CO_2 adsorption capacity, indicating that the construction of the heterojunction enhances the absorption of CO_2.

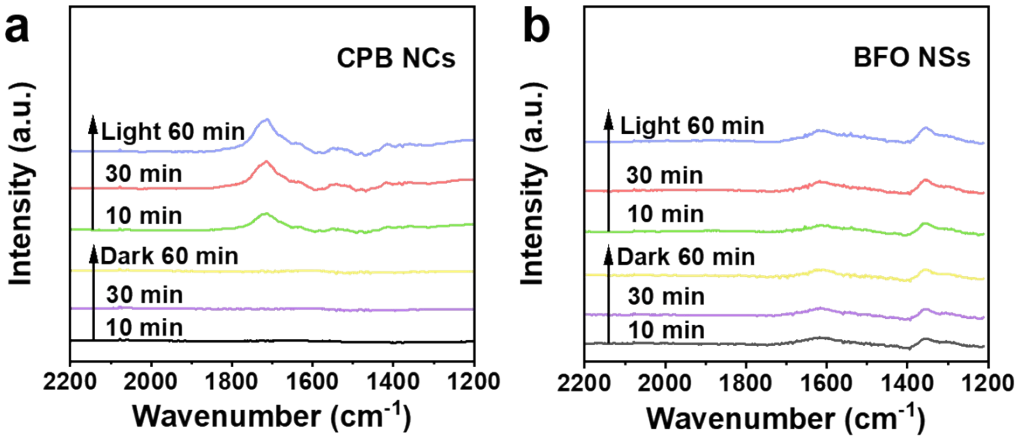

Fig. S17 *In-situ* FTIR spectra of CPB NCs and BFO NSs.

As shown in Fig. S16b, no signal for the intermediate was detected on the BFO NSs, which further indicates that the reaction occurred on the CPB NCs.

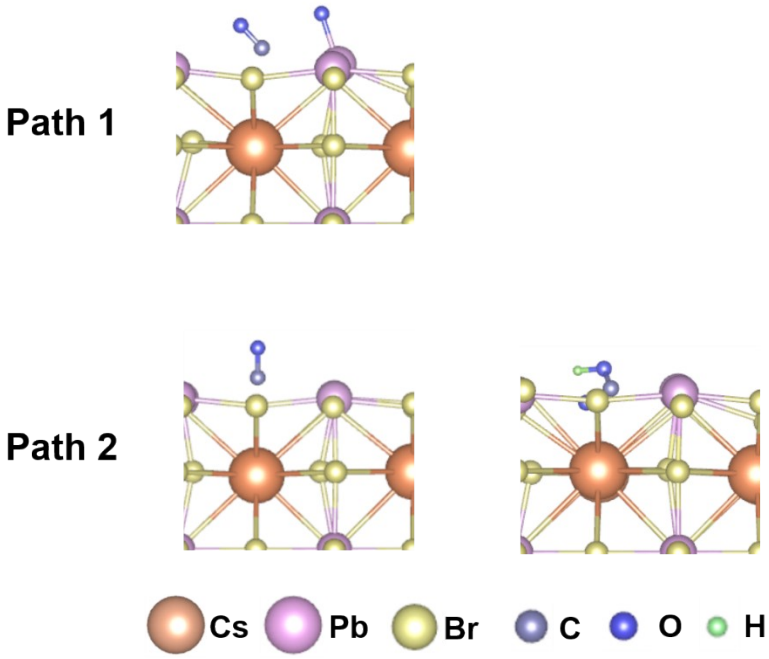

Fig. S18 Side views of the optimized structures for the intermediates on $CsPbBr_3$ during the two possible paths of CO_2 dissociative adsorption.

Table S1. A summary of the photocatalytic CO_2 reduction performance by various perovskite photocatalysts in a solid-gas system. To assure the comparability between different sources, the reaction rates are presented as rates of electron consumption.

Photocatalyst	Conditions	Light source	Products	$R_{electron}$ (μmol $g^{-1}h^{-1}$)	Ref
$BiFeO_3$/$CsPbBr_3$	Gas (CO_2+H_2O)	300 W Xe lamp, 150 mW cm^{-2}, λ>420 nm	CO, CH_4	106.2	**This work**
WO_3/$CsPbBr_3$/ZIF-67	Gas (CO_2+H_2O)	150 W Xe lamp, AM 1.5G, 150 mW cm^{-2}	CO, CH_4	70.22	[5]
m-CN@$CsPbBr_3$	Gas (CO_2+H_2O)	300W Xe lamp	CO	85.6	[6]
$CsPbBr_3$-Cu-RGO	Gas (CO_2+H_2O)	300W Xe lamp	CO, CH_4	103	[7]
MIL-100 (Fe)/ $CsPbBr_3$	Gas (CO_2+H_2O)	300W Xe lamp, full spectrum	CO	40.8	[8]
α-Fe_2O_3/RGO/ $CsPbBr_3$	Gas (CO_2+H_2O)	150 W Xe lamp, 150 mW cm^{-2}, λ>420 nm	CO, CH_4, H_2	81.0	[9]
Ni: $CsPbBr_3$-xAcx NC	Gas (CO_2+H_2O)	300 W Xe lamp, 100 mW cm^{-2}, λ>400 nm	CO	88.2	[10]
$CsPbBr_3$ NCs/ ZnO/RGO	Gas (CO_2+H_2O)	150 W Xe lamp, 150 mW cm^{-2}, λ>420 nm	CO, CH_4	52.0	[11]
Fe: $CsPbBr_3$	Gas (CO_2+H_2O)	450 W Xe lamp, 150 mW cm^{-2}	CO, CH_4	55.0	[12]
3-$Cs_4CuSb_2Cl_{12}$	Gas (CO_2+H_2O)	300W Xe lamp	CO, CH_4	36.1	[13]
14MA$PbBr_3$/$La_2Ti_2O_7$	Gas (CO_2+H_2O)	300 W Xe lamp, λ>400 nm	CO	12.6	[14]
$Cs_3Bi_2I_9$/Bi_2WO_6	Gas (CO_2+H_2O)	300 W Xe lamp, 100 mW cm^{-2}, λ>400 nm	CO	14.7	[15]
FA$PbBr_3$/PbI_2	Gas (CO_2+H_2O)	300 W Xe lamp, 100 mW cm^{-2}, λ>400 nm	CO, CH_4	29.3	[16]
MA$PbBr_3$/Pb-MOF	Gas (CO_2+H_2O)	300W Xe lamp	CO, CH_4	58.9	[17]

The rate of electron consumption for photocatalytic reduced product ($R_{electron}$) = 2R(CO) + 8R(CH_4) + 2R(H_2), where R(CO), R(CH_4) and R(H_2) are the formation rates (μmol g^{-1} h^{-1}) of the CO, CH_4,

and H_2, respectively.

Table S2. Fitting parameters of TRPL curves of pristine CPB, BFO/CPB heterojunction and the mixture of BFO and CPB.

Samples	A_1	A_2	τ_1	τ_2	τ_{avg}
CPB NCs	0.75	0.25	2.17	21.65	17.14
Mixture	0.78	0.22	1.76	13.61	9.88
BFO/CPB	0.85	0.15	1.22	8.47	5.21

The decay curves were fitted using a double-exponential decay kinetic:

$$Y = B + A_1\exp(-t/\tau_1) + A_2\exp(-t/\tau_2)$$

The average PL life times (τ_{avg}) were calculated according to the following equation:

$$\tau_{avg} = (A_1\tau_1^{\ 2} + A_2\tau_2^{\ 2})/ (A_1\tau_1 + A_2\tau_2)$$

Reference

1 L. Liu, H. Meng, Y. Chai, X. Chen, J. Xu, X. Liu, W. Liu, D. M. Guldi and Y. Zhu, *Angew. Chem. Int. Ed., 2023, **62**, e202217897.*

2 J. H. Shah, B. Huang, A. M. Idris, Y. Liu, A. S. Malik, W. Hu, Z. Zhang, H. Han and C. Li, *Small*, 2020, **16,** 2003361.

3 M. L. Xu, M. Lu, G. Y. Qin, X. M. Wu, T. Yu, L. N. Zhang, K. Li, X. Cheng and Y. Q. Lan, *Angew. Chem. Int. Ed., 2020, **61**, e202210700.*

4 Z. Chen, M. Z. Shahid, X. Jiang, M. Zhang, D. Pan, H. Xu, G. Jiang, J. Wang and Z. Li, *Small*, 2023, 2304756.

5 Y. J. Dong, Y. Jiang, J. F. Liao, H. Y. Chen, D. Bin Kuang and C. Y. Su, *Sci. China Mater.*, 2022, **65**, 1550–1559.

6 H. Bian, D. Li, S. Wang, J. Yan and S. Liu, *Chem. Sci.*, 2022, **13**, 1335–1341.

7 S. Kumar, M. Regue, M. A. Isaacs, E. Freeman and S. Eslava, *ACS Appl. Energy Mater.*, 2020, **3**, 4509–4522.

8 R. Cheng, E. Debroye, J. Hofkens and M. B. J. Roeffaers, *Catalysts*, 2020, **10**, 1–13.

9 Y. Jiang, J. F. Liao, H. Y. Chen, H. H. Zhang, J. Y. Li, X. D. Wang and D. Bin Kuang, *Chem*, 2020, **6**, 766–780.

10 J. Cheng, Y. Mu, L. Wu, Z. Liu, K. Su, G. Dong, M. Zhang and T. Lu, *Nano Res.*, 2022, **15**, 1845–1852.

11 Y. Jiang, J. F. Liao, Y. F. Xu, H. Y. Chen, X. D. Wang and D. Bin Kuang, *J. Mater. Chem. A*, 2019, **7**, 13762–13769.

12 S. Shyamal, S. K. Dutta and N. Pradhan, *J. Phys. Chem. Lett.*, 2019, **10**, 7965–7969.

13 K. Zhang, Y. Zhang, D. Zhou, Y. Yang, Z. Yang, Z. Song, J. Zhang, Q. Wang and J. Qiu, *J. Alloys Compd.*, 2024, **976**, 173283.

14 L. Yin, Z. Wang, D. Zhou, F. Guo, X. Zhang and K. Li, *New J. Chem.*, 2023, **47**, 20708–20712.

15 Z. L. Liu, R. R. Liu, Y. F. Mu, Y. X. Feng, G. X. Dong, M. Zhang and T. B. Lu,

Sol. RRL, 2021, **5**, 1–9.

16 N. N. Guo, Z. L. Liu, Y. F. Mu, M. R. Zhang, Y. Yao, M. Zhang and T. B. Lu, *Chinese Chem. Lett.*, 2022, **33**, 3039–3042.

17 D. Y. Zhou, W. T. Su, X. Y. Li, T. Hong, G. Y. Pan, M. L. Xu, F. T. Liu and K. Li, *J. Mater. Chem. C*, 2023, **11**, 15700–15705.